Shear-wave manipulation by embedded soft devices

Linli Chen, Chao Ma, Shiheng Zhao, Pingping Zheng, Qian Zhao, Zheng Chang *

College of Science, China Agricultural University, Beijing 100083, China

ARTICLE INFO

ABSTRACT

In accordance with hyperelastic transformation theory, a range of shear-wave manipulation devices can be designed with neo-Hookean materials pre-deformed properly. However, how such devices fit the background medium remains elusive. In this study, a systematic formula is developed in terms of elastic wave transmission and reflection between un-deformed and pre-deformed hyperelastic materials. By both theoretical analyses and numerical simulations, the shear-wave propagation from an un-deformed neo-Hookean material to the pre-deformed one is investigated. Among the three typical deformations, "constrained" uniaxial tension and simple-shear are found to be able to ensure total transmission, whereas ordinary uniaxial tension and hydrostatic compression could cause reflection. Thus, three embedded shear-wave manipulation devices are proposed, namely, a unidirectional cloak, a splicing beam bend and a concave lens; their performance is verified by numerical simulations. This study may underpin the design and realization of soft-matter-based wave control devices. Potential applications can be expected in nondestructive testing, impact protection, biomedical imaging, as well as soft robotics.

© 2020 Elsevier Ltd. All rights reserved.

1. Introduction

Elastic waves refer to mechanical vibrations propagating in solid media. As a carrier of energy and information, they have been extensively studied over centuries (Auld, 1973; Achenbach, 2012) and suggested technologically significant applications in numerous branches of engineering (e.g., nondestructive testing, medical imaging and geophysical prospecting). In recent years, hyperelastic soft materials (e.g., elastomers and gels) have aroused huge attention in elastodynamics (Bertoldi and Boyce, 2008; Norris and Parnell, 2012; Guo et al., 2017; Li et al., 2017; Xin and Lu, 2017; Deng et al., 2019; Zhang et al., 2019) for their high sensitivity, diverse material behavior, and reversible geometry effects exerted by finite deformation. It is noteworthy that a hyperelastic transformation theory (HTT) (Norris and Parnell, 2012) has been proposed, revealing that the soft materials with specified strain energy functions (SEFs) act as smart metamaterials (Shin et al., 2012) and can exhibit some unique wave manipulation properties by regulating their deformation. Note that in neo-Hookean materials, shear-wave (S-wave) paths comply with the distorted material curves (Chang et al., 2015). The mentioned finding inspires researchers to design considerable S-wave control devices (e.g., invisibility cloak (Parnell et al., 2012; Zhang and Parnell, 2018; Guo et al., 2019), wave mode splitter (Chang et al., 2015) and phononic

crystal (Liu et al., 2017; Zhang and Parnell, 2017)). As compared with the conventional transformation technique (Pendry et al., 2006; Rahm et al., 2008; Norris and Shuvalov, 2011), HTT does not require microstructures. Thus, such soft devices exhibit remarkable potential in non-dispersion and broadband wave manipulation. Moreover, compared with "hard" devices, such soft devices are naturally superior in integration with other soft-systems and may provide new insights into the designs of biomedical and soft robotic technologies.

On the whole, a soft device does not work as an individual, while it always embeds in its "working environment" or the background medium. In existing studies (Parnell et al., 2012; Guo et al., 2019), external boundaries of the finite soft devices are usually fixed, ensuring impedance matching between the soft device and the background. However, it also confines the possible finite deformation into a narrow range, thereby significantly limiting the functions that can be achieved by the soft device. If the constraint is relaxed, the discontinuity will occur at the interface between the soft device and the background. It is critical to clarify how the discontinuous interface affects the wave propagation. Open questions also cover how to find appropriate deformations by which the pre-deformed material can fit the background, and how to design soft devices exhibiting both the wave control capacity and the impedance matching property.

The small-on-large theory (Ogden, 2007) creates a natural framework to analyze the problem of incremental linear wave motions superimposed onto a finite pre-deformation. It lays an

---

essential basis for the soft device design and investigating their matching properties. In the theory, however, pre-deformed hyperelastic material usually exhibits an effective anisotropy and the behavior of a Cosserat-like continuum (Ogden, 1984). In this scenario, the classical theory (Auld, 1973) for elastic wave transmission and reflection becomes invalid. The principle that dictates such a physical process remains unknown.

To address the mentioned problems, in this paper, we present a systematic formulation of the transmission and reflection of elastic waves between un-deformed and pre-deformed hyperelastic materials. To be specific, we investigate S-wave propagating between an un-deformed neo-Hookean material, as well as the one subject to several typical deformations (e.g., uniaxial tension, hydrostatic compression, and simple-shear). On that basis, three embedded soft devices are proposed, namely, a unidirectional cloak, a splicing beam bend, and a concave lens. Furthermore, both theoretical analyses and numerical simulations are conducted to demonstrate the efficiency of such devices.

The rest of this paper is arranged as follows. In Section 2, the small-on-large theory is briefly reviewed as preliminary. In Section 3, the transmission and reflection of elastic waves between un-deformed and pre-deformed hyperelastic materials are analyzed. Next, the transmission characteristics of the S-wave are delved into at the interface of the neo-Hookean materials. In Section 4, three soft devices are proposed for S-wave manipulation. Lastly, our brief concluding remarks are drawn, and a discussion on the avenues for future work is presented in Section 5.

2. Small-on-large theory: Linear elastic wave propagation in a finitely deformed hyperelastic material

2.1. Large deformation

In terms of a hyperelastic solid with constitutive behavior characterized by the strain energy function W, the large (finite) deformation makes the material particle at X_j in the reference (un-deformed) configuration move to the current position x_i in the current (deformed) configuration. The large deformation (free of body force) follows the static equilibrium equation of (Ogden, 1984)

$$S_{ij,i} = 0 \tag{1}$$

where $S_{ij} = \partial W / \partial F_{ji}$ denotes the nominal (first Piola-Kirchoff) stress tensor; $F_{ji} = \partial x_j / \partial X_i$ is the deformation gradient. In Eq. (1) and beyond, the repeated subscripts imply summation over all possible values. By substituting the relation

$$C_{ijkl} = \frac{\partial S_{ij}}{\partial F_{lk}} = \frac{\partial^2 W}{\partial F_{ji} \partial F_{lk}} \tag{2}$$

into Eq. (1), the equilibrium equation can be rewritten as

$$(C_{ijkl} x_{l,K})_{,i} = 0 . \tag{3}$$

It is noteworthy that on the whole, the fourth-order elastic tensor C_{ijkl} is non-linearly determined by the deformation gradient F_{ij}. Accordingly, Eq. (3) refers to a set of quasi-linear partial differential equations of the second order for x_i (Ogden, 1984). In terms of a particular x_i (or equivalently F_{ij}), the uniquely determined elastic tensor C_{ijkl} is termed as the instantaneous elastic tensor expressed in the initial configuration. In this scenario, both C_{ijkl} and x_i are required to analyze the incremental wave motion.

2.2. Small wave motion

The incremental wave motion u_i superimposed onto the finite deformation x_i complies with

$$(C_{0ljKl} u_{l,K})_{,I} = \rho_0 \ddot{u}_j , \tag{4}$$

in the time domain, or

$$(C_{0ljKl} u_{l,K})_{,I} = -\omega^2 \rho_0 u_j , \tag{5}$$

in the frequency domain. C_{0ljKl} and ρ_0 denote the instantaneous elastic tensor and mass density obtained by a pushing forward operation on C_{ijkl} and ρ, respectively, i.e., (Ogden, 2007)

$$C_{0ljKl} = J^{-1} F_{li} F_{Kk} C_{ijkl}, \ \rho_0 = J^{-1} \rho , \tag{6}$$

where $J = \det(F_{ij})$ denotes the volumetric ratio.

For a homogeneously deformed hyperelastic material, incremental plane waves can be expressed as

$$u_i = A m_i e^{i(k l_j X_j - \omega t)}, \tag{7}$$

where A is the scalar wave amplitude, m_i denotes a unit polarization vector, i denotes $\sqrt{-1}$, k is the wave number, l_i represents the unit vector in the wave direction and ω is the angular frequency. By substituting Eq. (7) into Eq. (4), the *Christoffel* equation can be obtained as (Auld, 1973)

$$C_{0ljKl} l_l l_K m_l = c^2 \rho_0 m_j, \tag{8}$$

where $c = \omega/k$ denotes the phase velocity of the elastic wave. For an in-plane problem, by solving the eigenvalue problem of Eq. (8), the phase velocities (V_P and V_S) and the polarization (m_i) of the longitudinal (P-) and shear (S-) waves can be calculated.

3. Transmission and reflection of elastic waves at the interface between un-deformed and pre-deformed hyperelastic materials

3.1. Theoretical formulae

For simplicity, the finite deformation is restricted in the assumption of plane-strain, i.e., the out-of-plane principal stretch $\lambda_3 \equiv 1$, and the in-plane incremental waves are considered only. In such a two-dimensional problem, plane elastic wave incidence is considered on a plane interface between un-deformed (Domain I, $\mathbf{F}$ = unit tensor) and pre-deformed (Domain II, $\mathbf{F} \neq$ unit tensor) hyperelastic materials (Fig. 1). The pre-deformation can be imposed by mechanical loading, or by any external field (e.g., heat (Kino et al., 2017; Bisoyi et al., 2019), electric field (Okuzaki et al., 2009; Haghiashtiani et al., 2018) or magnetic field (Kankanala and Triantafyllidis, 2004; Zhao et al., 2019)) introduced to hyperelastic materials responding to such stimuli. However, such external
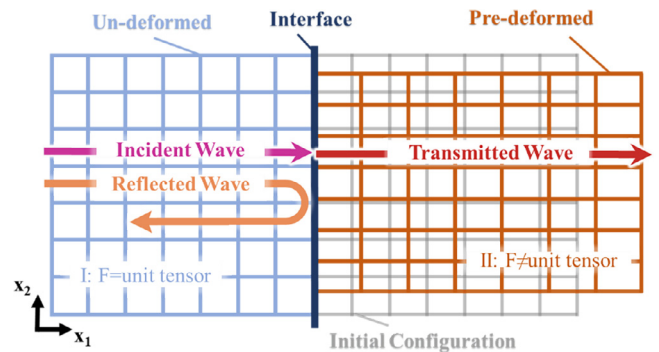

Fig. 1. Schematic diagram of an elastic wave propagations from an un-deformed hyperelastic material (I, light blue mesh) to a pre-deformed one (II, orange mesh). A normal incidence is considered at the interface (dark blue line). Besides, the initial configuration (gray mesh) of the pre-deformed material is presented as a reference.

loading mechanisms should be carefully designed to avoid the possible impact on wave propagation. With the loaded state being maintained, the deformed material is perfectly bonded to the undeformed one. In this study, the normal incidence is considered to avoid mode conversion (Auld, 1973) induced by oblique incidence. Meantime, in the theoretical analysis, the deformation in Domain II is restricted as homogeneous, so the elastic waves travel in straight paths.

At the interface, the particle velocity $v_i = \partial u_i / \partial t$ and the traction of the *Cauchy* stress $\sigma_{ij} = C_{0ijkl} u_{l,k}$ induced from the elastic wave motion $\boldsymbol{u}$ should be continuous, which are expressed as,

$$v_i^{\text{I}} = v_i^{\text{II}}, \tag{9}$$

$$\sigma_{ij}^{\text{I}} n_j = \sigma_{ij}^{\text{II}} n_j, \tag{10}$$

in which n_j is the unit normal vector. An S-wave is considered propagating along the direction of $l_1 = 1$, $l_2 = 0$ (Fig. 1) and polarizing in the direction of $m_1 = 0$, $m_2 = 1$. According to Eqs. (7) and (8), and with the time harmonicity $e^{i(kl_1 X_1 - \omega t)}$ being omitted, in Domain I, the particle velocity and the traction at the interface ($X_1 = 0$) are expressed as

$$\left(v_2^{\text{I}}\right)_{inc} = A, \quad \left(\sigma_{21}^{\text{I}}\right)_{inc} = i\omega A \rho V_{\text{S}}, \tag{11}$$

where the subscript *inc* represents the incident wave, the subscript $i = 1, 2$ denotes the component of the spatial coordinate X_i. Likewise, the particle velocity and the stress of the P- and S-waves emerged at the interface are expressed as

$$\left(v_1^{\text{I}}\right)_R = B, \quad \left(\sigma_{11}^{\text{I}}\right)_R = -i\omega B \rho V_{\text{P}}^{\text{I}}, \tag{12}$$

$$\left(v_2^{\text{I}}\right)_R = C, \quad \left(\sigma_{21}^{\text{I}}\right)_R = -i\omega C \rho V_{\text{S}}^{\text{I}}, \tag{13}$$

$$\left(v_{1'}^{\text{II}}\right)_T = D, \quad \left(\sigma_{1'1'}^{\text{II}}\right)_T = i\omega D \rho_0 V_{\text{P}}^{\text{II}}, \tag{14}$$

$$\left(v_{2'}^{\text{II}}\right)_T = E, \quad \left(\sigma_{2'1'}^{\text{II}}\right)_T = i\omega E \rho_0 V_{\text{S}}^{\text{II}}, \tag{15}$$

where the subscripts R and T respectively represent the reflection and the transmitted waves, the subscript $i' = 1'$, $2'$ denotes the polarization direction $m_{i'}$ in Domain II, while B, C, D and E refer to the scalar amplitudes of the waves.

For the equivalent anisotropy resulting from the finite deformation, quasi-mode elastic waves may exist (Chen et al., 2017), which means that the P- and S-waves' polarization directions in Domain II are no longer parallel or normal to the directions of propagation. Thus, φ is introduced as the angle between the polarization vectors in Domain I and II. In this regard, Eqs. (14) and (15) can be expressed as the spatial coordinate X_i by using (Auld, 1973)

$$\begin{bmatrix} v_1^{\text{II}} \\ v_2^{\text{II}} \end{bmatrix} = \begin{bmatrix} \cos\varphi & -\sin\varphi \\ \sin\varphi & \cos\varphi \end{bmatrix} \begin{bmatrix} v_{1'}^{\text{II}} \\ v_{2'}^{\text{II}} \end{bmatrix}, \tag{16}$$

and

$$\begin{bmatrix} \sigma_{11}^{\text{II}} \\ \sigma_{21}^{\text{II}} \end{bmatrix} = \begin{bmatrix} \cos\varphi & -\sin\varphi \\ \sin\varphi & \cos\varphi \end{bmatrix} \begin{bmatrix} \sigma_{1'1'}^{\text{II}} \\ \sigma_{2'1'}^{\text{II}} \end{bmatrix}. \tag{17}$$

By substituting Eqs. (11)–(15) into Eq. (9), it yields

$$B = D\cos\varphi - E\sin\varphi, \tag{18}$$

$$A + C = D\sin\varphi + E\cos\varphi. \tag{19}$$

Likewise, Eq. (10) can be written as

$$B\rho V_{\text{P}}^{\text{I}} = -D\rho_0 V_{\text{P}}^{\text{II}}\cos\varphi + E\rho_0 V_{\text{S}}^{\text{II}}\sin\varphi, \tag{20}$$

$$-A\rho V_{\text{S}}^{\text{I}} + C\rho V_{\text{S}}^{\text{I}} = -D\rho_0 V_{\text{P}}^{\text{II}}\sin\varphi - E\rho_0 V_{\text{S}}^{\text{II}}\cos\varphi. \tag{21}$$

By solving Eqs. (18)–(21), the transmission and reflection coefficients Γ_{ns}^m are defined as

$$\Gamma_{\text{TP}}^{\text{S}} = \frac{D}{A} = \frac{2\rho V_{\text{S}}^{\text{I}}\sin\varphi\left(\rho_0 V_{\text{S}}^{\text{II}} + \rho V_{\text{P}}^{\text{I}}\right)}{\Delta}, \tag{22}$$

$$\Gamma_{\text{TS}}^{\text{S}} = \frac{E}{A} = \frac{2\rho V_{\text{S}}^{\text{I}}\cos\varphi\left(\rho V_{\text{P}}^{\text{I}} + \rho_0 V_{\text{P}}^{\text{II}}\right)}{\Delta}, \tag{23}$$

$$\Gamma_{\text{RP}}^{\text{S}} = \frac{B}{A} = -\frac{2\rho\rho_0 V_{\text{S}}^{\text{I}}\sin\varphi\cos\varphi\left(V_{\text{P}}^{\text{II}} - V_{\text{S}}^{\text{II}}\right)}{\Delta}, \tag{24}$$

$$\begin{aligned} \Gamma_{\text{RS}}^{\text{S}} &= \frac{C}{A} \\ &= \frac{\rho^2 V_{\text{S}}^{\text{I}} V_{\text{P}}^{\text{I}} - \rho_0^2 V_{\text{S}}^{\text{II}} V_{\text{P}}^{\text{II}} + \rho\rho_0\sin^2\varphi\left(V_{\text{S}}^{\text{I}} V_{\text{S}}^{\text{II}} - V_{\text{P}}^{\text{I}} V_{\text{P}}^{\text{II}}\right) + \rho\rho_0\cos^2\varphi\left(V_{\text{S}}^{\text{I}} V_{\text{P}}^{\text{II}} - V_{\text{S}}^{\text{II}} V_{\text{P}}^{\text{I}}\right)}{\Delta}, \end{aligned} \tag{25}$$

where $\Delta = \rho^2 V_{\text{S}}^{\text{I}} V_{\text{P}}^{\text{I}} + \rho_0^2 V_{\text{S}}^{\text{II}} V_{\text{P}}^{\text{II}} + \rho\rho_0\sin^2\varphi\left(V_{\text{S}}^{\text{I}} V_{\text{S}}^{\text{II}} + V_{\text{P}}^{\text{I}} V_{\text{P}}^{\text{II}}\right) + \rho\rho_0\cos^2\varphi\left(V_{\text{S}}^{\text{I}} V_{\text{P}}^{\text{II}} + V_{\text{S}}^{\text{II}} V_{\text{P}}^{\text{I}}\right)$. For Γ_{ns}^m, the superscript $m = $ P, S denotes the incident wave mode, while the subscripts $n = $ T, R and $s = $ P, S respectively represent the transmitted and reflected waves and the corresponding wave modes.

Likewise, for P-wave incidence, the transmission and reflection coefficients are defined as

$$\Gamma_{\text{TP}}^{\text{P}} = \frac{2\rho V_{\text{P}}^{\text{I}}\cos\varphi\left(\rho_0 V_{\text{S}}^{\text{II}} + \rho V_{\text{S}}^{\text{I}}\right)}{\Delta}, \tag{26}$$

$$\Gamma_{\text{TS}}^{\text{P}} = -\frac{2\rho V_{\text{P}}^{\text{I}}\sin\varphi\left(\rho V_{\text{S}}^{\text{I}} + \rho_0 V_{\text{P}}^{\text{II}}\right)}{\Delta}, \tag{27}$$

$$\Gamma_{\text{RP}}^{\text{P}} = \frac{\rho^2 V_{\text{S}}^{\text{I}} V_{\text{P}}^{\text{I}} - \rho_0^2 V_{\text{S}}^{\text{II}} V_{\text{P}}^{\text{II}} + \rho\rho_0\sin^2\varphi\left(V_{\text{P}}^{\text{I}} V_{\text{P}}^{\text{II}} - V_{\text{S}}^{\text{I}} V_{\text{S}}^{\text{II}}\right) + \rho\rho_0\cos^2\varphi\left(V_{\text{S}}^{\text{II}} V_{\text{P}}^{\text{I}} - V_{\text{S}}^{\text{I}} V_{\text{P}}^{\text{II}}\right)}{\Delta}, \tag{28}$$

$$\Gamma_{\text{RS}}^{\text{P}} = -\frac{2\rho\rho_0 V_{\text{P}}^{\text{I}}\sin\varphi\cos\varphi\left(V_{\text{P}}^{\text{II}} - V_{\text{S}}^{\text{II}}\right)}{\Delta}. \tag{29}$$

3.1.1. A particular case: S-wave incidence in a neo-Hookean material

In the following, as an example of the mentioned theory, as well as the theoretical basis for developing a neo-Hookean transformation device, the transmission and reflection of an S-wave between an un-deformed neo-Hookean material and a pre-deformed one are taken into account. The three-dimensional SEF of the neo-Hookean material (Bertoldi and Boyce, 2008; Chang et al., 2015) is simplified into a two-dimensional form as (Chen et al., 2017)

$$W = \frac{\lambda}{2}(J - 1)^2 - \mu\ln(J) + \frac{\mu}{2}(I_1 - 2), \tag{30}$$

where I_1 denotes the first invariant of the right *Cauchy-Green* tensor, and λ and μ are the *Lamé* constants. Such a simplified form can effectively analyze the propagation of in-plane elastic waves in hyperelastic materials exhibiting finite plane-strain deformations.

Note that the P- and S-waves propagate in a pre-deformed neo-Hookean material in their pure modes (Chen et al., 2017). Accordingly, with $\varphi = 0$, Eq. (22)-(25) are simplified as

$$\Gamma_{\text{TP}}^{\text{S}} = 0, \tag{31}$$

$$\Gamma_{\text{TS}}^{\text{S}} = \frac{2\rho V_{\text{S}}^{\text{I}}}{\rho V_{\text{S}}^{\text{I}} + \rho_0 V_{\text{S}}^{\text{II}}}, \tag{32}$$
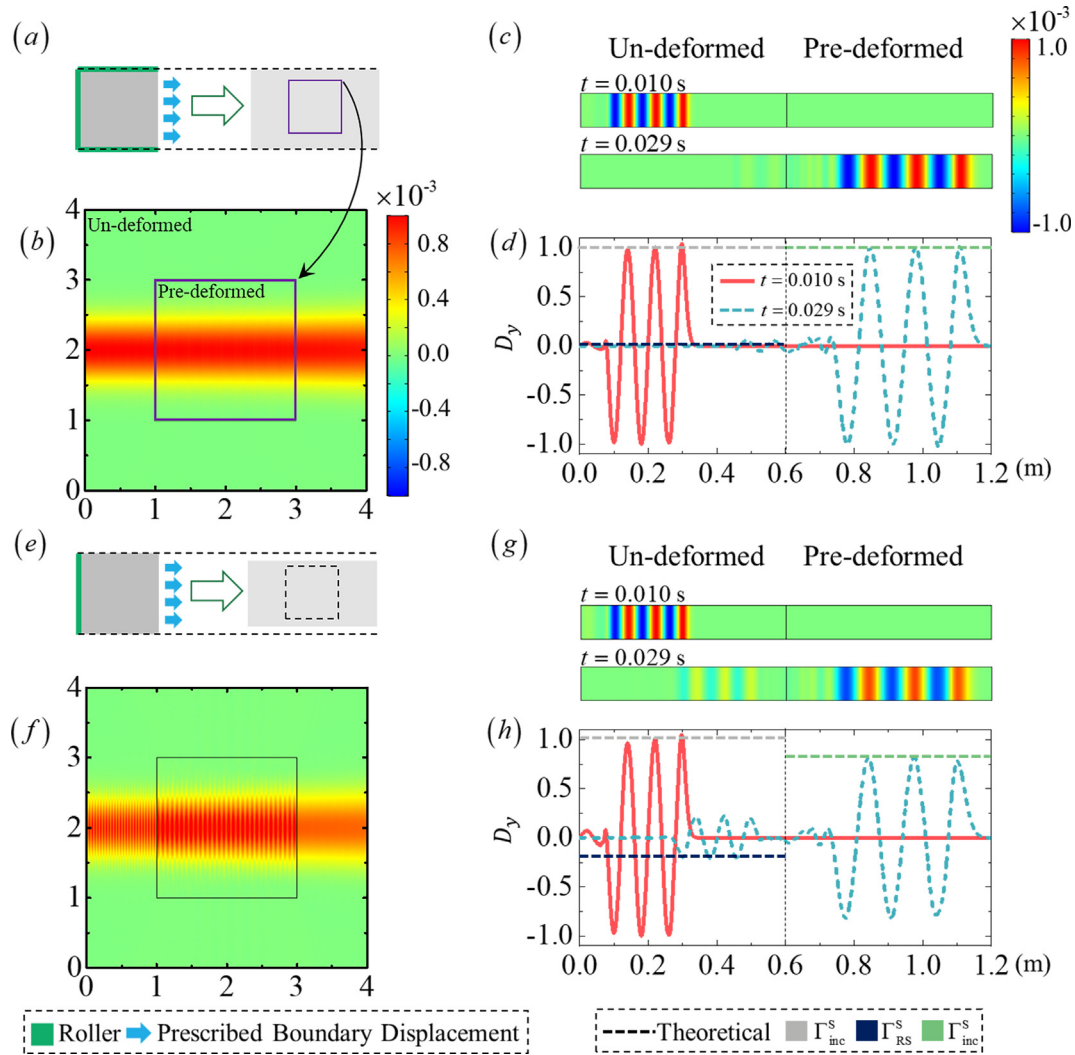
Fig. 2. Transmission and reflection of elastic waves at the interfaces between un-deformed and uniaxial-tensioned hyperelastic materials. (a)-(d), "constrained" uniaxial-tension; (e)–(h), "ordinary" uniaxial-tension. (a) and (e) represent the schematic diagrams of the deformation modes, the dark and light grey zones represent the un-deformed and pre-deformed hyperelstic material, respectively. (b) and (f) illustrate the steady-state displacement fields of $|u_2|$, when the shear-wave beams are incident on the square pre-deformed domains. (c) and (g) refer to the transient-state normalized displacement fields of D_2 at $t = 0.01$ s and $t = 0.029$ s on the left (un-deformed) and right (pre-deformed) sides of the interface. Moreover, (d) and (h) depict the amplitudes of D_2 at the two snapshots, together with the theoretical results of Γ_{inc}^{S}, Γ_{RS}^{S}, Γ_{TS}^{S}.

$$\Gamma_{RP}^{S} = 0, \tag{33}$$

$$\Gamma_{RS}^{S} = \frac{\rho V_S^I - \rho_0 V_S^{II}}{\rho V_S^I + \rho_0 V_S^{II}}. \tag{34}$$

Eq. (31) and (33) indicate that no P-wave is generated during the S-wave transmission. Eqs. (32) and (34) suggest that $\Gamma_{TS}^{S} - \Gamma_{RS}^{S} = 1$ and $\Gamma_{RS}^{S} \leq 0$. The negative reflection coefficient is attributed to the half-wave loss, revealing that the wave receives a 180° phase shift.

3.2. Numerical method

To verify the mentioned theoretical results and the performances of the subsequent soft devices, numerical simulations are performed by a two-step model with the software COMSOL Multiphysics.

First, the finite deformation of a hyperelastic material, complying with Eq. (1), is calculated with the module of structural mechanics. As a result, the deformed geometry, together with the deformation gradient F_{ij}, is substituted into the wavefield analysis.

Second, i.e., the wavefield analysis, both steady-state and transient-state analyses are conducted. On the whole, the steady-state analysis intuitively suggests the wavefield distribution and the direction of wave propagation, while the transient-state analysis clearly differentiates the incident and reflected waves.

In the steady-state analysis, Eq. (5) is modeled with the module of weak form PDE (Eriksson et al., 1996) to address the asymmetry of the elastic tensor C_{0IjKl} (Eq. (6)). A portion of pre-deformed neo-Hookean material or a designed soft device (with F_{ij} calculated in the first step) is embedded in an un-deformed neo-Hookean domain, as an example demonstrated in Fig. 2(b). On the periphery of the un-deformed domain, perfectly matched layers (Chang et al., 2014) (not shown) are adopted to avoid unnecessary reflection. An S-wave Gaussian beam is introduced at an appropriate location as required.

In the transient-state analysis, the module of weak form PDE is also employed to solve Eq. (4). Fig. 2(c) indicates that two rectangular domains act as the un-deformed and pre-deformed neo-Hookean domains. A temporally bounded pulse of plane S-wave with the excitation lasting for three wavelengths is imported at the left boundary. The upper and lower boundaries are set as
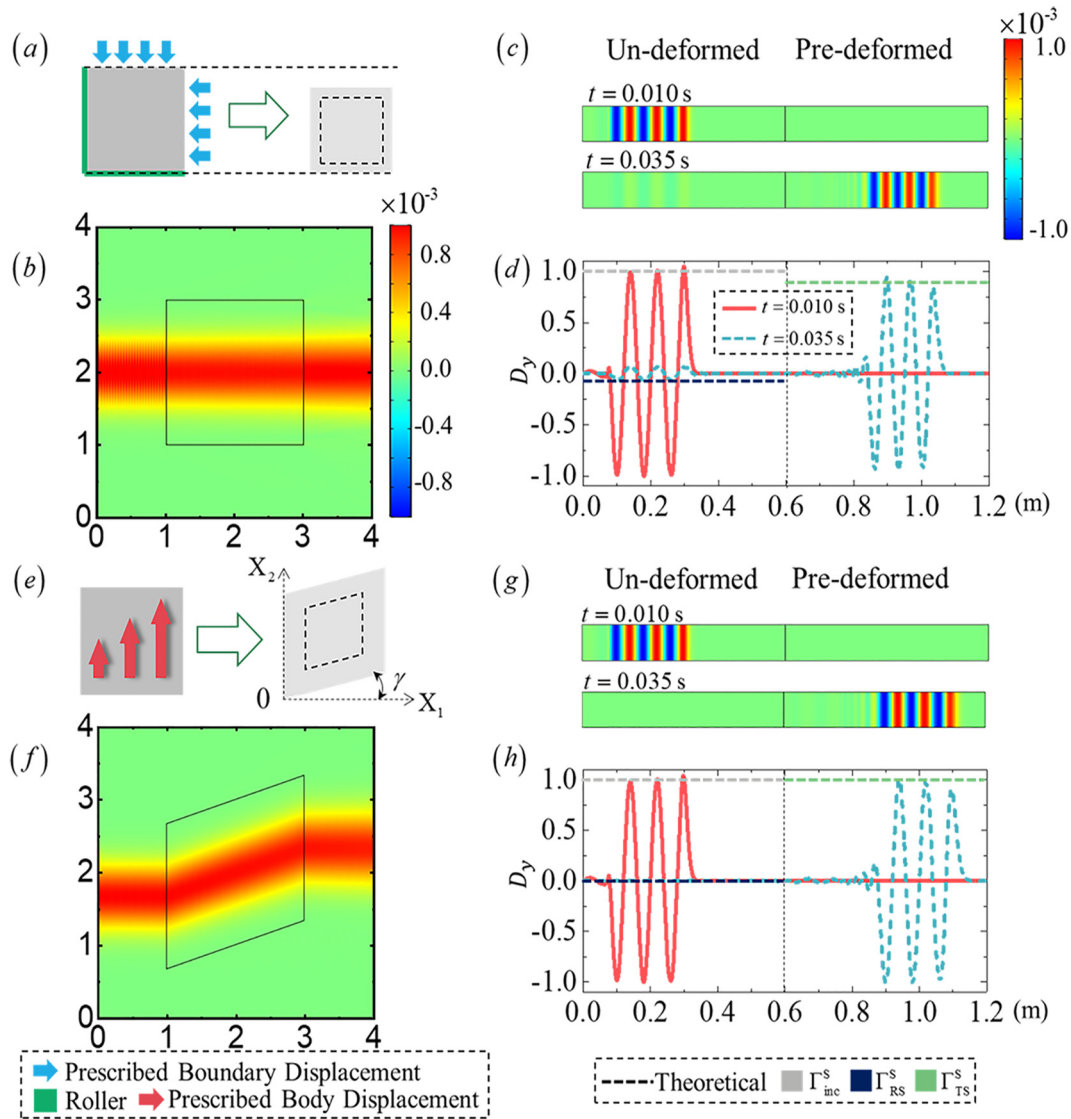
Fig. 3. Transmission and reflection of elastic waves at the interfaces between un-deformed hyperelastic material and the one subject to (a)-(d) hydrostatic compression and (e)–(h) simple-shear. (a) and (e) represent the implementation schemes of the deformation modes, the dark and light grey zones represent the un-deformed and pre-deformed hyperelstic material, respectively. (b) and (f) denote the steady-state displacement fields of $|u_2|$, when the shear-wave beams are incident on the square pre-deformed domains. (c) and (g) indicate the transient-state normalized displacement fields of D_2 at $t = 0.01$ s and $t = 0.035$ s on the left (un-deformed) and right (pre-deformed) sides of the interface. Moreover, (d) and (h) depict the amplitudes of D_2 at the two snapshots, together with the theoretical results of Γ_{inc}^S, Γ_{RS}^S, and Γ_{TS}^S.

Floquet-Bloch periodic (Bloch, 1929), and the right boundary is not constrained.

In all the following numerical simulations, $\lambda = 4.32$ MPa, $\mu = 1.08$ MPa, and $\rho = 1050$ kg/m^3 are taken as the initial material parameters of the neo-Hookean material, referring to a compressible variant of material PSM-4 (Bertoldi and Boyce, 2008). For all the wave modes, the amplitude of the wave source is set to $A = 0.01$ m. In steady-state analyses, the angular frequencies are set to $\omega_{st} = 3$ kHz to avoid the divergence of the Gaussian beams. In contrast in transient-state analyses, a much lower frequency $\omega_{tr} = 0.4$ kHz is adopted to clearly show the amplitude of the waves.

3.3. Particular cases for the pre-deformation

To gain some prior knowledge to design the soft device, three typical deformations (namely, uniaxial tension, hydrostatic compression, and simple-shear) are theoretically delved into. Numerical simulations are also performed to confirm the theoretical results. More importantly, the validated numerical procedure can

then be followed to address inhomogeneous deformation where the analytical approach is incapable.

3.3.1. Uniaxial tension

In the first case, the hyperelastic materials subject to uniaxial tension are considered. The deformation can be achieved by applying a displacement $x_1 - X_1 = 0.667a$ m on the right boundary of an a m $\times a$ m ($a \geq 2$) square hyperelastic material, with the rest boundaries set as rollers (Fig. 2(a)). For such "constrained" uniaxial tension, the components of the deformation gradient are $F_{11} = 1.667$, $F_{22} = 1$ and $F_{12} = F_{21} = 0$. As a result, the elongation ratio in X_1-direction reaches $\eta = 1.667$.

With the pre-deformation being maintained, a 2 m $\times$ 2 m square (Fig. 2(a)) is cut out of the material and slotted into the (un-deformed) background, as shown in Fig. 2(b). In terms of an S-wave horizontally propagating through a portion of the pre-deformed neo-Hookean material, the steady-state displacement field $|u_2|$ is illustrated in Fig. 2(b). This figure presents that the S-wave is not altered by the two interfaces it passes through,
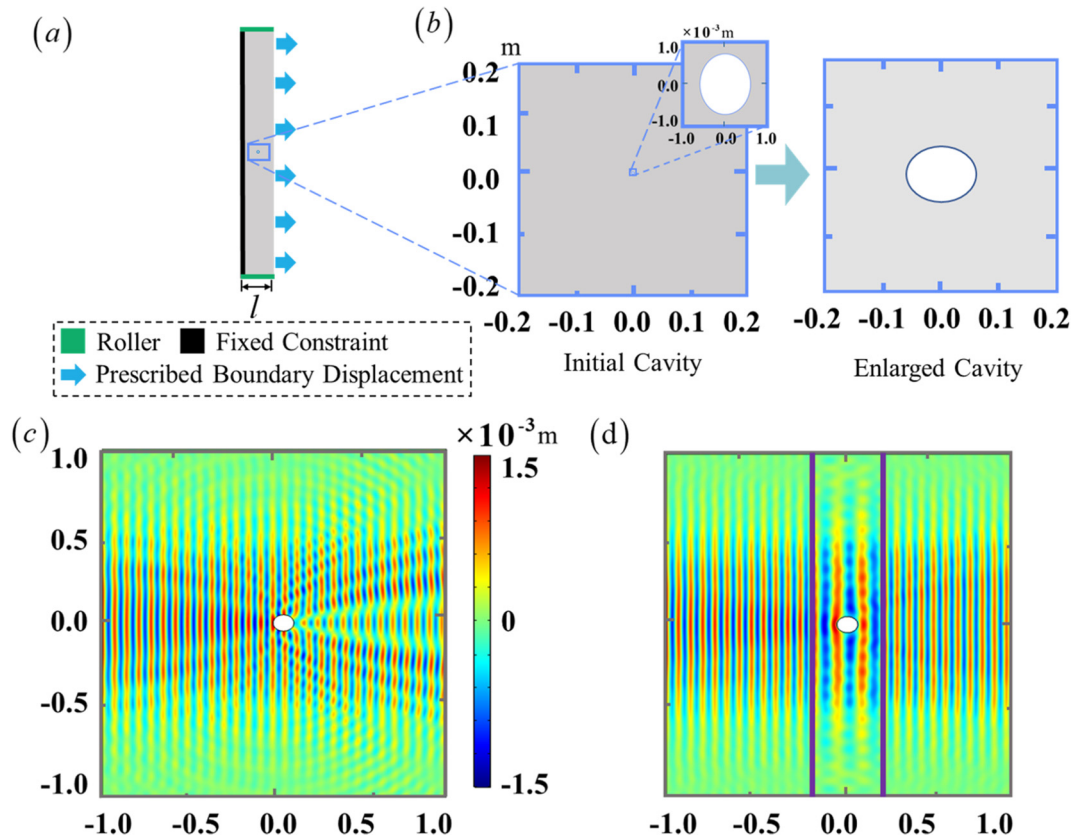
Fig. 4. Schematic diagram and performance of the unidirectional cloak. (a) The implementation scheme of the unidirectional cloak. (b) A magnified view of the initial and enlarged cavities. (c) and (d) Displacement field u_2 in neo-Hookean material with and without the unidirectional cloak (purple line) for the incidence of an S-wave beam: (c) uncloaked case: a cavity without cloak. (b) cloaked case: a cavity with a cloak of $\eta = 2$.

revealing that the "constrained" uniaxial tensioned neo-Hookean material perfectly match with the un-deformed one. Such numerical result complies with the theoretical calculation obtained by Eq. (34) and Eq. (32), i.e., $\Gamma_{TS}^S = 1$ and $\Gamma_{RS}^S = 0$. According to the transient-state analysis, two typical snapshots ($t = 0.01$ s and $t = 0.029$ s) of the normalized displacement field $D_2 = u_2/A$ are presented in Fig. 2(c). D_2 distributions along the X_1-direction in the two snapshots are illustrated in Fig. 2(d), of which the theoretical results are marked as horizontal dashed lines. It is therefore indicated that the wavelength in the deformed domain at $t = 0.029$ s is $\eta = 1.667$ times of that in the un-deformed one at $t = 0.01$ s. After the wave impinges at the interface, no backward wave is generated.

If the upper and lower roller constrains in the "constrained" uniaxial tension are relaxed, the uniaxial tension becomes an "ordinary" one (Fig. 2(e)). Then, the components of the deformation gradient turn as $F_{11} = 1.667$, $F_{22} = 0.685$, and $F_{12} = F_{21} = 0$. In this case, the perfect matching ceases to exist. As revealed from the steady-state wave field demonstrated in Fig. 2(f), as impacted by the superposition of incident and reflected waves, the pre-deformed neo-Hookean material exhibits higher field strength than that in the un-deformed domain. The mismatch is illustrated in the transient-state analysis (Fig. 2(g) and (h)). At $t = 0.029$ s, the transmitted wave exhibits a significantly lower amplitude than the incident one, and the reflection can be identified in the un-deformed domain. Both the steady-state and transient-state analyses demonstrate the theoretical results $\Gamma_{TS}^S = 0.813$ and $\Gamma_{RS}^S = -0.187$.

3.3.2. Hydrostatic compression

In the second scenario, the hydrostatic compression is considered. For a square neo-Hookean domain exhibiting a side length of

$a \, (\geq 2)$ m, the deformation can be achieved with the left and lower boundaries set to be rollers; meantime, the upper and right boundaries are set to the prescribed displacements of $x_1 - X_1 = x_2 - X_2 = -0.125a$ m (Fig. 3(a)). Accordingly, the components of the deformation gradient are expressed as $F_{11} = F_{22} = 0.875$ and $F_{12} = F_{21} = 0$. Though it is unlikely to be preserved in the steady-state wave field (Fig. 3(b)), the transient result (Fig. 3(c) and (d)) indicates a slight impedance mismatch, as assessed by the theoretical results $\Gamma_{TS}^S = 0.933$ and $\Gamma_{RS}^S = -0.067$.

3.3.3. Simple-shear

In the third scenario, simple-shear deformation is considered. As demonstrated in Fig. 3(e), the deformation can be achieved with the prescribed body displacement $x_2 - X_2 = X_1/3$ mon the square material domain, and the components of the deformation gradient are $F_{11} = F_{22} = 1$, $F_{21} = 0.333$ and $F_{12} = 0$ correspondingly. Fig. 3(f) indicates that the wave beam has been shifted together with the simple-shear deformation, revealing the S-wave manipulation capability of the neo-Hookean material. Meantime, no reflection takes place when the wave beam is propagating through the material (Fig. 3(f)–(h)).

4. Embedded neo-Hookean transformation devices for S-wave manipulation

The mentioned theoretical and numerical investigations can direct the design of embedded soft devices exhibiting tunable properties. Here "tunable" implies that the performance of the soft devices can be conveniently regulated by applying deformations of different degrees on the identical soft material. Next, three devices are proposed as examples.
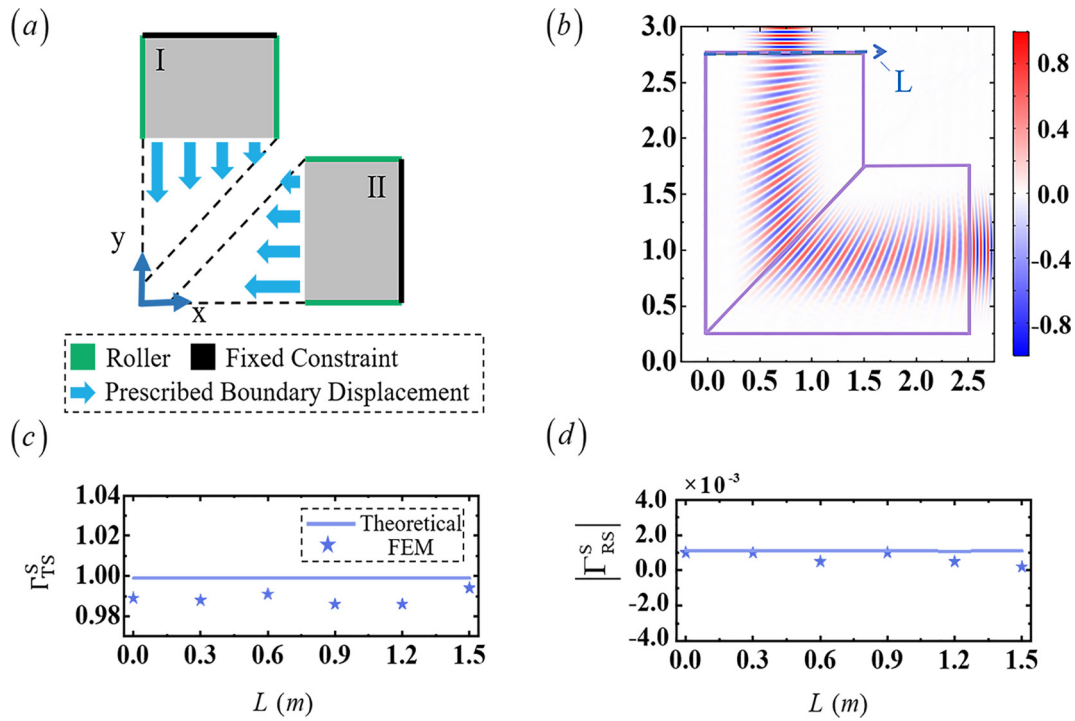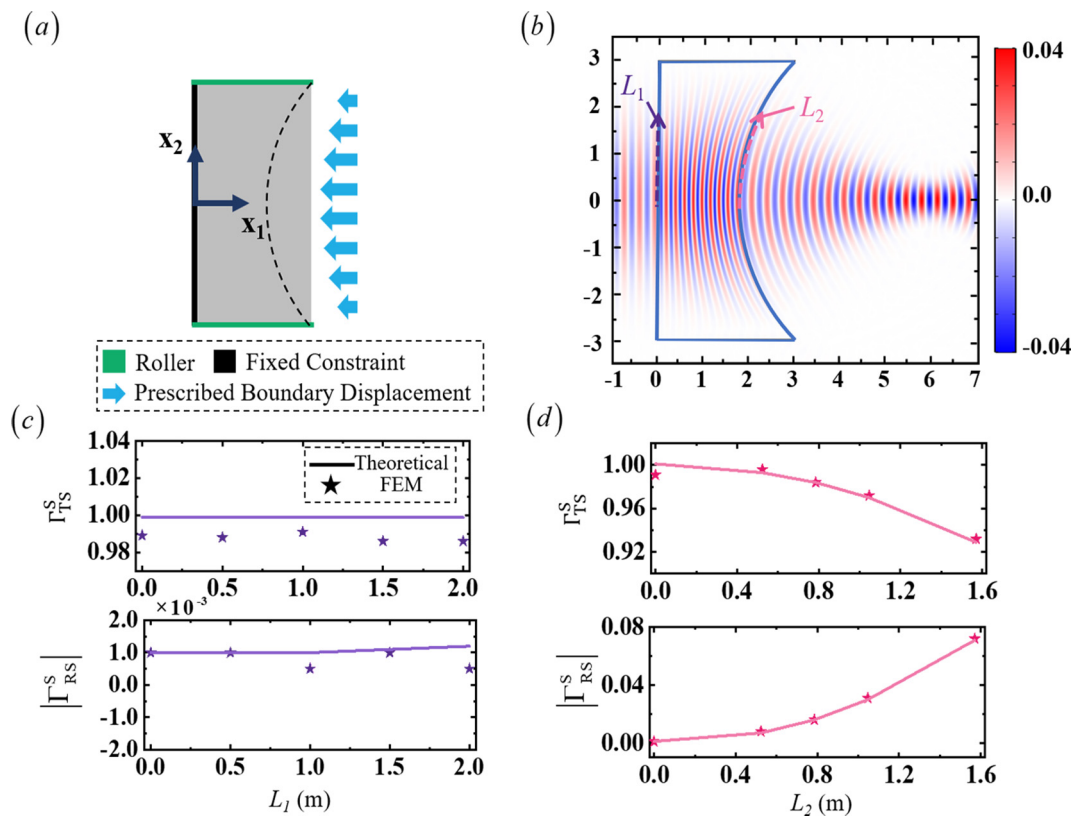
Fig. 5. Schematic diagram and performance of the splicing beam bend. (a) The implementation scheme of the beam bend. (b) The curl field in and out of the beam bend when an S-wave beam incident takes place in $-X_2$-direction. (c) and (d) Numerical simulation and theoretical prediction of the transmission $\left(\Gamma_{TS}^{S}\right)$ and reflection $\left(\left|\Gamma_{RS}^{S}\right|\right)$ coefficients of the micro-elements, on auxiliary segment L_1 presented in (b).

Fig. 6. Schematic diagram and performance of the concave lens. (a) The implementation scheme of the lens. (b) The curl field in and out of the lens when an S-wave beam incident takes place in X_1-direction. (c) and (d) respectively represent the numerical simulation and theoretical prediction of the transmission $\left(\Gamma_{TS}^{S}\right)$ and reflection $\left(\left|\Gamma_{RS}^{S}\right|\right)$ coefficients of the micro-elements on auxiliary segments L_1 and L_2.

4.1. Unidirectional cloak

To suppress the scattering of a cavity in a neo-Hookean material, a neo-Hookean material under "constrained" uniaxial tension with the enlarge ratio η (Fig. 4(a)) is embedded into a rectangular domain around the cavity. In such unidirectional cloak, a tiny cavity is set in the proper position, so it can enlarge to the identical size as the target cavity we want to conceal (Fig. 4(b)). On the left and right boundaries far from the cavity, the homogeneous "constrained" uniaxial stress state ensures the reflectionless of the cloak.

In the numerical simulation, an S-wave beam is horizontally impinging on an elliptical cavity with its two semi-axes $a = 57.20$ mm and $b = 47.27$ mm. In this scenario, Fig. 4(c) presents the distribution of the displacement u_2 of the total elastic field, indicating a significance scattering. As a result, the displacement field of a cloaked cavity is illustrated in Fig. 4(d). With the size of the initial elliptical cavity set to $a_0 = 0.67$ mm and $b_0 = 0.83$ mm, the target cavity can be obtained by applying a "constrained" uniaxial tension with the enlarge ratio $\eta = 2$ on a neo-Hookean layer with initial width $l = 0.2$ m (Fig. 4(a)). The reflectionless of the cloak on its left and right interfaces are significantly identified. Meantime, the wavelength turns out to be η times as long as the original one in the cloak region. The u_2 field out of the cloak region appears to be considerably smoother than that in the case without the cloak. According to HTT, it is predictable that the larger the elongation ratio η, the more effectively the scattering will be suppressed.

4.2. Splicing beam bend

By invoking HTT, an S-wave beam bend can be achieved by bending a rectangular neo-Hookean material to a certain angle. However, under the large angle, and the aspect ratio of the rectangle is relatively small, instability and damage may happen in the soft material. To avoid such failure, a splicing beam bend is proposed, by which a significantly huge bending angle can be reached by assembling several moderately deformed components. Fig. 5(a) gives a schematic diagram of a splicing $\pi/2$ - bend. The beam bend consists of two identical trapezoid components, each of which is achieved by fixing one of the long sides of a rectangular neo-Hookean material with length $l = 1.5$ m and width $d = 1$ m and exploiting an appropriate boundary displacement (e.g., $x_2 - X_2 = X_1 - 1.5$ m for the component I, Fig. 5(a)) to the opposite side. Meantime, the two short sides are constrained with rollers.

The curl field of an S-wave beam propagates through the beam bend is illustrated in Fig. 5(b), suggesting an ideal wave manipulation. At the seam of the two components of the beam bend, material properties are identical, so no reflection takes place. At both the inlet and outlet interfaces, the deformations are inhomogeneous. To characterize the matching properties, the transmission and reflection coefficients of six infinitesimal micro-elements on the inlet (L_1 in Fig. 5(b)) are plotted in Fig. 5(c) and (d). Both theoretical results and numerical simulations reveal that the transmission coefficient is universally close to 1, while the reflection coefficient is negligible. Through polar decomposing for the deformation gradient ($F_{11} = 1.81$, $F_{12} = -2.01 \times 10^{-6}$, $F_{21} = 0.336$ and $F_{22} = 1$) at $(0.875, 2.75)$, i.e., the midpoint of L_1, the micro-element is reported a "constrained" uniaxial-tensioned one ($\eta = 1.81$), with a negligible rotation angle of $2.1 \times 10^{-4}\pi$.

4.3. Concave lens

In the last example, a concave lens is proposed, thereby focusing a plane S-wave to a point and then converting a plane wave

into a cylindrical one. A rectangular neo-Hookean material with width $l = 3$ m and hight $d = 6$ m is considered. As depicted in Fig. 6(a), the left boundary is fixed and the upper and lower boundaries are constrained with rollers. To focus the wave at $(6, 0)$ m from the lens (Fig. 6(b)), a displacement of $x_1 - X_1 = 3 - \sqrt{18 - X_2^2}$ m is applied at the right boundary of the neo-Hookean domain.

According to the curl field plotted in Fig. 6(b), the horizontally propagated wave beam is concentrated at the expected position. The transmission and reflection coefficients on micro-elements of the two interfaces (L_1 and L_2 in Fig. 6(b)) where the wave beam passes through are ascertained. By adopting a similar deformation mode as the mentioned beam bend, the micro-elements on L_1 indicate an approximate match with the background (Fig. 6(c)). However, along L_2, mismatch takes places away from the axis of symmetry (Fig. 6(d)). 8% of the transmission loss can be identified at 1.6 m away from the axis of symmetry. Nevertheless, the performance of the lens can be ensured with the satisfactory transmission coefficient in the region where the beam energy is primarily distributed.

5. Conclusion and discussion

In this study, a systematic formulation of the transmission and reflection of elastic waves between un-deformed and pre-deformed hyperelastic materials is presented. As the problem is equated with transmission and reflection between isotropic and anisotropic medium with and without Cosserat form, the formulation may also find applications in other engineering fields (e.g., geophysics (Thomsen, 1988; Malehmir and Schmitt, 2017)).

It is suggested that the neo-Hookean material with the SEF of Eq. (30) exhibits an outstanding character in the soft device design, since the elastic waves propagate in the neo-Hookean material in pure-modes. On that basis, to make the S-wave device fit the background, "constrained" uniaxial tension or simple-shear deformation at the interface (perfect match) is recommended to be exploited. Alternatively, it is also feasible to keep the input and output interfaces un-deformed (perfect match) or deformed as small as possible (approximate match). Though all the three devices proposed here comply with "constrained" uniaxial tension, one case of simple-shear deformation can be referenced in a design of wave-mode splitter in a previous contribution (Chang et al., 2015).

We hope this study may inspire a series of further research. In this study, we only consider in-plane elastic waves. How the discontinuity result from the finite deformation affects the anti-plane wave motion (Parnell, 2012; Zhang and Parnell, 2018) is also worthy of investigation. It is also expected that if different hyperelastic models, various background medium, and arbitrary incidence angle of elastic waves are considered, more sophisticated but fruitful results can be anticipated. This may also provide more freedom to design wave control devices with soft materials. This work also promotes an interesting and challenging direction for material fabrication. With the development of modern chemical synthesis processes, more elaborate theory and methodology are needed to precisely fabricate a material based on the criteria of a particular SEF. Lastly, the viscoelastic effect of the material is neglected here. Existing studies (Dykstra et al., 2019; Parnell and De Pascalis, 2019) revealed that the effect is critical to shear waves in rubber-like materials. Thus, a low-damping hyperelastic material or other mechanisms to generate large deformation with low wave attenuation (Goldsberry et al.,2019) is required in practical applications.

Hopefully, this study may also provide some novel insights into energy and information transmission in such fields as in non-

destructive testing, impact protection, biomedical imaging, or soft robotics.

Declaration of Competing Interest

The authors declare that they do not have any known competing financial interests or personal relationships that could have appeared to influence the work reported in this paper.

Acknowledgement

References

Achenbach, J., 2012. Wave Propagation in Elastic Solids. Elsevier.

Auld, B.A., 1973. Acoustic Fields and Waves in Solids. Wiley.

Bertoldi, K., Boyce, M.C., 2008. Wave propagation and instabilities in monolithic and periodically structured elastomeric materials undergoing large deformations. Phys. Rev. B 78, 184107.

Bisoyi, H.K., Urbas, A.M., Li, Q., 2019. Soft materials driven by photothermal effect and their applications. Photoactive Functional Soft Materials: Preparation, Properties, and Applications, 1–44.

Bloch, F., 1929. Über die quantenmechanik der elektronen in kristallgittern. Z. Phys. 52, 555–600.

Chang, Z., Guo, D., Feng, X.-Q., Hu, G., 2014. A facile method to realize perfectly matched layers for elastic waves. Wave Motion 51, 1170–1178.

Chang, Z., Guo, H.-Y., Li, B., Feng, X.-Q., 2015. Disentangling longitudinal and shear elastic waves by neo-Hookean soft devices. Appl. Phys. Lett. 106, 161903.

Chen, L., Chang, Z., Qin, T., 2017. Elastic wave propagation in simple-sheared hyperelastic materials with different constitutive models. Int. J. Solids Struct. 126–127, 1–7.

Deng, B., Zhang, Y., He, Q., Tournat, V., Wang, P., Bertoldi, K., 2019. Propagation of elastic solitons in chains of pre-deformed beams. New J. Phys. 21, 073008.

Dykstra, D.M.J., Busink, J., Ennis, B., Coulais, C., 2019. Viscoelastic Snapping Metamaterials. J. Appl. Mech. 86.

Eriksson, K., Estep, D., Hansbo, P., Johnson, C., 1996. Computational differential equations. Cambridge University Press.

Goldsberry, B.M., Wallen, S.P., Harberman, M.R., 2019. Non-reciprocal wave propagation in mechanically-modulated continuous elastic metamaterials. J. Acoust. Soc. Am. 146, 782–788.

Guo, D., Chang, Z., Hu, G., 2019. In-Plane Semi-Linear Cloaks with Arbitrary Shape. Acta Mech. Solida Sin. 32, 277–286.

Guo, D., Chen, Y., Chang, Z., Hu, G., 2017. Longitudinal elastic wave control by pre-deforming semi-linear materials. J. Acoust. Soc. Am. 142, 1229–1235.

Haghiashtiani, G., Habtour, E., Park, S.-H., Gardea, F., McAlpine, M.C., 2018. 3D printed electrically-driven soft actuators. Extreme Mech. Lett. 21, 1–8.

Kankanala, S., Triantafyllidis, N., 2004. On finitely strained magnetorheological elastomers. J. Mech. Phys. Solids 52, 2869–2908.

Kino, H., Samrejfuangfoo, N., Tsuda, K., Kato, T., Fujioka, H., Miyamoto, N., 2017. Fundamental study of soft actuator using anisotropic gel hybridized with nanosheet liquid crystal: analysis of heat characteristics and length control. Proc. Comput. Sci. 105, 62–67.

Li, G.-Y., He, Q., Mangan, R., Xu, G., Mo, C., Luo, J., Destrade, M., Cao, Y., 2017. Guided waves in pre-stressed hyperelastic plates and tubes: Application to the ultrasound elastography of thin-walled soft materials. J. Mech. Phys. Solids 102, 67–79.

Liu, Y., Chang, Z., Feng, X.-Q., 2017. Stable elastic wave band-gaps of phononic crystals with hyperelastic transformation materials. Extreme Mech. Lett. 11, 37–41.

Malehmir, R., Schmitt, D.R., 2017. Acoustic reflectivity from variously oriented orthorhombic media: Analogies to seismic responses from a fractured anisotropic crust. J. Geophys. Res.: Solid Earth 122, 10,069-010,085.

Norris, A.N., Parnell, W.J., 2012. Hyperelastic cloaking theory: transformation elasticity with pre-stressed solids. Proc. Roy. Soc. A: Math. Phys. Eng. Sci. 468, 2881–2903.

Norris, A.N., Shuvalov, A.L., 2011. Elastic cloaking theory. Wave Motion 48, 525–538.

Ogden, R.W., 1984. Non-linear elastic deformations. Ellis Horwood.

Ogden, R.W., 2007. Incremental statics and dynamics of pre-stressed elastic materials. Cism Courses Lect, 1–26.

Okuzaki, H., Suzuki, H., Ito, T., 2009. Electrically driven PEDOT/PSS actuators. Synth. Met. 159, 2233–2236.

Parnell, W.J., 2012. Nonlinear pre-stress for cloaking from antiplane elastic waves. Proc. Roy. Soc. A: Math. Phys. Eng. Sci. 468, 563–580.

Parnell, W.J., De Pascalis, R., 2019. Soft metamaterials with dynamic viscoelastic functionality tuned by pre-deformation. Philos. Trans. Roy. Soc. A 377, 20180072.

Parnell, W.J., Norris, A.N., Shearer, T., 2012. Employing pre-stress to generate finite cloaks for antiplane elastic waves. Appl. Phys. Lett. 100, 171907.

Pendry, J.B., Schurig, D., Smith, D.R., 2006. Controlling electromagnetic fields. Science 312, 1780–1782.

Rahm, M., Cummer, S.A., Schurig, D., Pendry, J.B., Smith, D.R., 2008. Optical design of reflectionless complex media by finite embedded coordinate transformations. Phys. Rev. Lett. 100, 063903.

Shin, D., Urzhumov, Y., Jung, Y., Kang, G., Baek, S., Choi, M., Park, H., Kim, K., Smith, D.R., 2012. Broadband electromagnetic cloaking with smart metamaterials. Nat. Commun. 3, 1–8.

Thomsen, L., 1988. Reflection seismology over azimuthally anisotropic media. Geophysics 53, 304–313.

Xin, F., Lu, T.J., 2017. Self-controlled wave propagation in hyperelastic media. Sci. Rep. 7, 7581.

Zhang, K., Ma, C., He, Q., Lin, S., Chen, Y., Zhang, Y., Fang, N.X., Zhao, X., 2019. Metagel with broadband tunable acoustic properties over air–water–solid ranges. Adv. Funct. Mater. 29, 1903699.

Zhang, P., Parnell, W.J., 2017. Soft phononic crystals with deformation-independent band gaps. Proc Math Phys Eng Sci 473, 20160865.

Zhang, P., Parnell, W.J., 2018. Hyperelastic antiplane ground cloaking. J. Acoust. Soc. Am. 143, 2878–2885.

Zhao, R., Kim, Y., Chester, S.A., Sharma, P., Zhao, X., 2019. Mechanics of hard-magnetic soft materials. J. Mech. Phys. Solids 124, 244–263.